

PointCore: Efficient Unsupervised Point Cloud Anomaly Detector Using Local-Global Features

Baozhu Zhao, Qiwei Xiong, Xiaohan Zhang, Jingfeng Guo, Qi Liu, *Senior Member, IEEE*, Xiaofen Xing, *Member, IEEE*, Xiangmin Xu, *Senior Member, IEEE*

Abstract—Three-dimensional point cloud anomaly detection that aims to detect anomaly data points from a training set serves as the foundation for a variety of applications, including industrial inspection and autonomous driving. However, existing point cloud anomaly detection methods often incorporate multiple feature memory banks to fully preserve local and global representations, which comes at the high cost of computational complexity and mismatches between features. To address that, we propose an unsupervised point cloud anomaly detection framework based on joint local-global features, termed PointCore. To be specific, PointCore only requires a single memory bank to store local (coordinate) and global (PointMAE) representations and different priorities are assigned to these local-global features, thereby reducing the computational cost and mismatching disturbance in inference. Furthermore, to robust against the outliers, a normalization ranking method is introduced to not only adjust values of different scales to a notionally common scale, but also transform densely-distributed data into a uniform distribution. Extensive experiments on Real3D-AD dataset demonstrate that PointCore achieves competitive inference time and the best performance in both detection and localization as compared to the state-of-the-art Reg3D-AD approach and several competitors.

Index Terms—3D point cloud, anomaly detection, unsupervised learning

I. INTRODUCTION

ANOMALY detection aims to find the abnormal region of products and plays an important role in various fields, such as industrial quality inspection [1], [2], and autonomous driving [3], [4]. Current anomaly detection methods [5]–[7] are mostly unsupervised and they target on two-dimensional (2D) images, where models are typically trained on images with well-studied architectures. For 3D point cloud-based anomaly detection task, there remains relatively unexplored within the current literature. Compared with 2D images, 3D point clouds have the advantage of richer structural information, which, however, gets along with but disorder, highly sparse and irregular distribution. To process point clouds distinctly, various handcrafted or deep learning-based feature descriptors at different scales are applied.

Recently, a large-scale, high-resolution 3D anomaly detection dataset, termed Real3D-AD [8], was provided. The objects in Real3D-AD dataset have 0.001mm-0.0015mm resolution, 360 degree coverage and perfect prototype. In [8], the authors applied PatchCore [9] from image anomaly detection to point

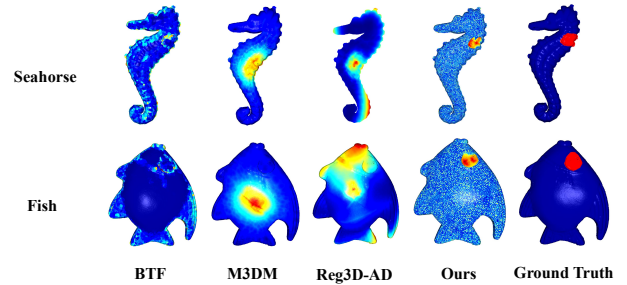


Fig. 1: Heatmaps of anomaly scores obtained by several methods on the Real3D-AD dataset. From the visualization, we see that the proposed method can detect and locate anomaly data points more accurately compared to others.

cloud anomaly detection, and developed a general-purpose registration-based point cloud anomaly detector, dubbed as Reg3D-AD. Reg3D-AD employs a dual-feature representation approach to preserve the local and global features of training prototypes, which achieves remarkable detection accuracy but slow inference. Current point cloud anomaly detectors can be categorized into twofolds: (1) Reconstruction-based methods, which reconstruct the input point cloud data via autoencoder [10]–[12] and identify anomalies by comparing the deviation between the original and reconstructed data. However, these approaches are sensitive to the resolution of point clouds, leading to slower inference speed and worse accuracy. (2) Memory bank-based approaches [8], [13], where memory banks are useful for storing representative features to implicitly build a normal distribution and looking for the out-of-distributed defects. Compared with the former, using a pretrained feature extractor directly to construct a memory bank enjoys fast training speed and is not affected by the resolution of point clouds. Besides that, existing point cloud anomaly detectors [8], [14] often incorporate multiple feature memory banks to fully preserve local and global representations, which comes at the high cost of computational complexity and mismatching between features.

To address the above issues, we propose an unsupervised point cloud anomaly detection framework based on joint local-global features, termed PointCore. To be specific, our contributions are summarized as follows:

1. PointCore only requires a memory bank to store local-global representations and different priorities are assigned to these local-global features to reduce the computational cost and mismatching disturbance for inference.

Corresponding author: Qi Liu (drluqi@scut.edu.cn)

B. Zhao, Q. Xiong, X. Zhang, J. Guo and X. Xu are with the School of Future Technology, South China University of Technology, China 511400

X. Xing is with the School of Electronic and Information Engineering, South China University of Technology, Guangzhou 510640, China.

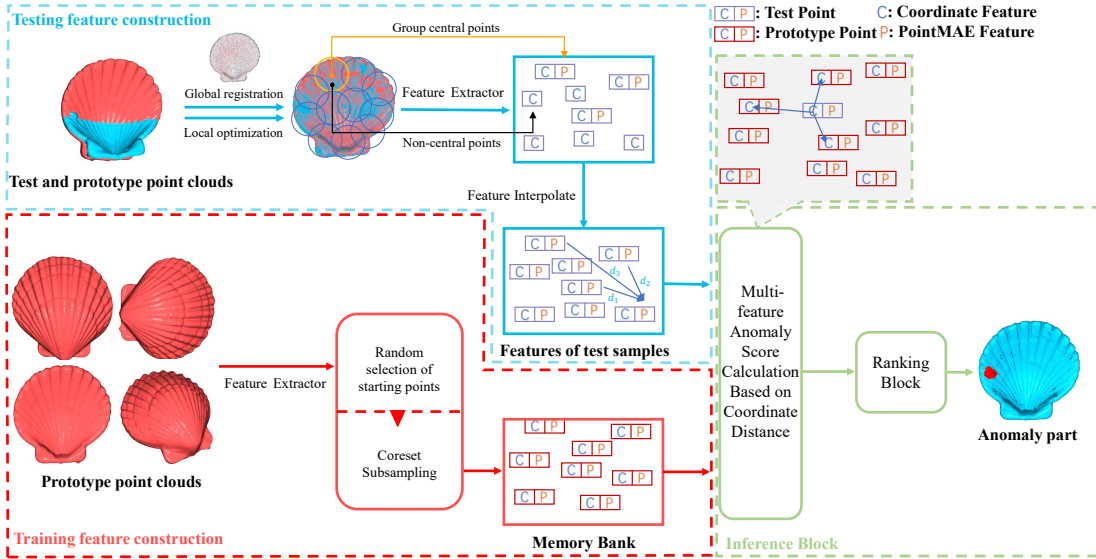


Fig. 2: **The pipeline of PointCore architecture.** We randomly select and convert template point clouds as the reference coordinates through global registration and local optimization methods, use pre-trained PointMAE feature extractor to obtain the PointMAE features, and then bind the coordinates and the features to establish the coordinate-PointMAE memory bank. Finally, we compute anomaly scores for all points in inference.

2. We propose a ranking-based normalization method to eliminate the distribution differences among various anomaly scores and apply the point-to-plane Iterative Closest Points(point-plane ICP) algorithm to perform local optimization of point cloud registration results for robust decision-making.
3. Extensive experiments on Real3D-AD dataset demonstrate that PointCore achieves competitive inference time and the best performance in both detection and localization as compared to the state-of-the-art Reg3D-AD approach and several competitors.

II. METHOD

A. Global and Local Registration

Similar to the Reg3D-AD model [8], we apply the FPFH [15] feature descriptor and the random sample consensus (RANSAC) algorithm to achieve global registration of point clouds. To enhance the stability of point cloud registration, a point-plane ICP [16] is introduced to locally optimize the outputs from global registration. Suppose two point clouds X_s (source point cloud) and X_t (target point cloud) need to be registered, the procedure is as follows:

- 1) Apply rotation matrix and translation vector obtained from the global registration to transform X_s .
- 2) Search q_i in X_t such that closest to p_i in X_s , where the normal vector of q_i is denoted as n_i .
- 3) Assume optimal rotation Euler angles $\alpha, \beta, \gamma \rightarrow 0$, we have $\cos(\theta) \rightarrow 1, \sin(\theta) \rightarrow 0, \theta \rightarrow 0$. The rotation matrix R can be approximately expressed as:

$$R \approx \begin{bmatrix} 1 & -\gamma & \beta \\ \gamma & 1 & -\alpha \\ -\beta & \alpha & 1 \end{bmatrix} \quad (1)$$

- 4) Assume the optimal translation vector is $t = [t_x, t_y, t_z]$. The loss function is shown as a least squares problem via Moore–Penrose inverse.

$$E(R, t) = \sum_{i=1}^n \left((Rp_i + t - q_i)^T n_i \right)^2 \quad (2)$$

- 5) Apply the computed rotation matrix and translation vector to transform X_s , and repeat steps 2-5 until the loss value is below a predefined threshold. Note that the target point cloud X_t for registration is fixed.

B. Memory Bank Construction

Coordinate Sampling. We employ a greedy down-sampling algorithm [17] to sample the point clouds. Given the point clouds X , and the point set C_a , a is the number of points in C_a . We aim to obtain S_{\max} uniform points from C_a . The specific procedure is as follows:

1. Randomly select S_{init} points from C_a to construct the initial point set $P_{\text{init}} = \{P_1, P_2, P_3, \dots, P_{S_{\text{init}}}\}$.
2. Calculate distances between C_a and P_{init} to obtain a matrix d_{2d} with dimensions $a \times S_{\text{init}}$.

$$d_{2d} = \begin{bmatrix} d_{11} & \cdots & d_{1S_{\text{init}}} \\ \vdots & \ddots & \vdots \\ d_{a1} & \cdots & d_{aS_{\text{init}}} \end{bmatrix}$$

3. Calculate the mean for each row of the matrix d_{2d} to obtain $d_{1d} = [d_{1\text{mean}}, d_{2\text{mean}} \cdots, d_{a\text{mean}}]$.
4. Locate the maximum value in the matrix d_{1d} , and add the corresponding point to P_{init} . Repeat steps 2-4 until the number of elements in P_{init} equals S_{\max} .

Point Feature Interpolation. A point transformer (PointMAE) [18], [19] pretrained on the ShapeNet [20] dataset is used as our 3D feature extractor. For each point cloud, we use coordinates from the coordinate sampling stage as the center

TABLE I: O-AUROC score for anomaly detection of all categories of Real3D-AD. Our method clearly outperforms other methods in most categories and has a huge advantage in average performance.

Category	BTF [14]		M3DM [21]		PatchCore [9]			PointCore	
	Raw	FPFH	PointMAE	FPFH	FPFH+Raw	PointMAE	PointMAE+Raw	FPFH+Raw	PointMAE+Raw
Airplane	0.730	0.520	0.434	0.882	0.848	0.726	0.716	0.792	0.660
Car	0.647	0.560	0.541	0.590	0.777	0.498	0.697	0.871	0.866
Candybar	0.539	0.630	0.552	0.541	0.570	0.663	0.685	0.861	0.976
Chicken	0.789	0.432	0.683	0.837	0.853	0.827	0.852	0.842	0.841
Diamond	0.707	0.545	0.602	0.574	0.784	0.783	0.900	0.847	0.963
Duck	0.691	0.784	0.433	0.546	0.628	0.489	0.584	0.642	0.684
Fish	0.602	0.549	0.540	0.675	0.837	0.630	0.915	0.915	0.993
Gemstone	0.686	0.648	0.644	0.370	0.359	0.374	0.417	0.477	0.535
Seahorse	0.596	0.779	0.495	0.505	0.767	0.539	0.762	0.954	0.973
Shell	0.396	0.754	0.694	0.589	0.663	0.501	0.583	0.853	0.882
Starfish	0.530	0.575	0.551	0.441	0.471	0.519	0.506	0.617	0.652
Toffees	0.703	0.462	0.450	0.565	0.626	0.585	0.827	0.728	0.929
Average	0.635	0.603	0.552	0.593	0.682	0.594	0.704	0.783	0.829

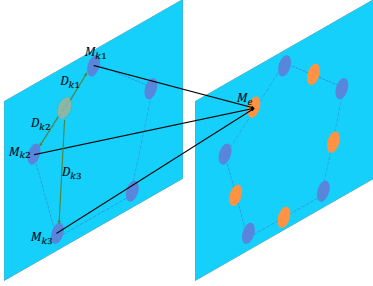


Fig. 3: The process of the PointMAE feature interpolation.

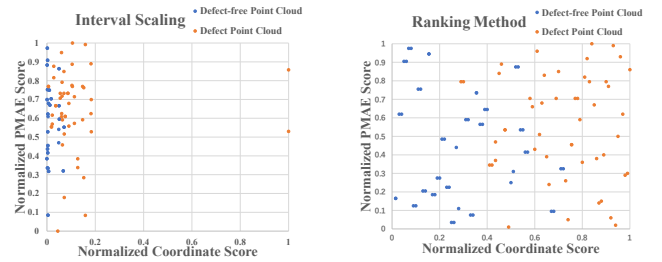
points of groups. Each central point forms a memory element, which is bound with coordinates and PointMAE features. These elements constitute the memory bank in Fig. 2. To reduce the computational complexity of PointMAE features computation in inference, it is necessary to downsample the point cloud coordinates. Therefore, we perform point feature interpolation further to assign a PointMAE feature value to each coordinate in the feature bank. The feature interpolation method is shown in Fig. 3.

Given a point set P_{central} with all center point coordinates, the corresponding PointMAE feature set is M_{init} . Taking a non-central point P_e as an example, we use the k -nearest neighbors algorithm to obtain three nearest neighbors $[P_{k1}, P_{k2}, P_{k3}]$ in the point set P_{central} . The corresponding Euclidean distances and PointMAE feature values are $[D_{k1}, D_{k2}, D_{k3}]$ and $[M_{k1}, M_{k2}, M_{k3}]$, respectively. By using eq. (3), we obtain the PointMAE feature M_e for P_e . This process is repeated until all non-central points obtain their corresponding PointMAE features. The M_e is computed by

$$M_e = \frac{D_{k1}D_{k2}M_{k3} + D_{k1}D_{k3}M_{k2} + D_{k2}D_{k3}M_{k1}}{D_{k1}D_{k2} + D_{k1}D_{k3} + D_{k2}D_{k3}} \quad (3)$$

C. Inference Block

Multi-feature Anomaly Score Calculation. The memory bank is composed of the element sets, that is, $M_{\text{train}} = \{(M_{1c}, M_{1p}), (M_{2c}, M_{2p}), \dots, (M_{nc}, M_{np})\}$, where M_{ic} denotes the coordinates of the i -th point, and M_{ip} represents the PointMAE feature of the i -th point. The test feature bank is



(a) Traditional normalization method. (b) Ranking-based normalization method.

Fig. 4: Distribution of coordinate and PointMAE anomaly scores normalized by these two methods.

defined as $F_{\text{test}} = \{(F_{1c}, F_{1p}), (F_{2c}, F_{2p}), \dots, (F_{mc}, F_{mp})\}$, where F_{jc} is the coordinates of the j -th point, and F_{jp} is the PointMAE feature of the j -th point. For an element (F_{jc}, F_{jp}) in F_{test} , we use its coordinate information F_{jc} to find three nearest neighbors in M_{train} , denoted as $\{(M_{ic}, M_{ip}), (M_{oc}, M_{op}), (M_{uc}, M_{up})\}$. Using Euclidean distance, their coordinate distances $\{DC_1, DC_2, DC_3\}$ and feature distances $\{DP_1, DP_2, DP_3\}$ are obtained. The final coordinate anomaly score is $S_c = \text{mean}(DC_1, DC_2, DC_3)$ and PointMAE anomaly score is $S_p = \min(DP_1, DP_2, DP_3)$.

Ranking Block. Due to the differences in scale and distribution between two anomaly scores, both scores are necessary to normalize. Traditional normalization often employs the interval scaling method. For a set of data S_{list} , the interval scaling process is $S_{\text{norm}} = \frac{S_{\text{list}} - \min(S_{\text{list}})}{\max(S_{\text{list}}) - \min(S_{\text{list}})}$. As depicted in Fig. 4, the interval scaling method will eliminate differences in scale between two anomaly scores but cannot address differences in distribution. When the coordinate anomaly score has two outliers, the final anomaly score will be much smaller than the PointMAE anomaly score. This has a significant impact on ensemble strategies based on arithmetic operations. To address that, we have designed a ranking-based normalization method, where $\text{Sort_rank}(S_{\text{list}})$ obtains the ranking of each value in S_{list} , and $\text{len}(S_{\text{list}})$ is the length of S_{list} . That is:

$$S_{\text{norm}} = \frac{\text{Sort_rank}(S_{\text{list}})}{\text{len}(S_{\text{list}})} \quad (4)$$

TABLE II: Comparing various metrics with the State of the Art (SOTA) model, which is Reg3D-AD (PatchCore+PointMAE+RAW), our model has achieved significant improvements across all metrics while substantially improving the inference speed.

Category	Reg3D-AD					PointCore				
	O-AUROC	P-AUROC	O-AUPR	P-AUPR	Time(s)	O-AUROC	P-AUROC	O-AUPR	P-AUPR	Time(s)
Airplane	0.716	0.631	0.703	0.017	17.759	0.66	0.608	0.667	0.016	5.737
Car	0.697	0.718	0.753	0.135	12.938	0.866	0.706	0.862	0.088	4.830
Candybar	0.827	0.724	0.824	0.109	11.241	0.976	0.760	0.973	0.322	1.743
Chicken	0.852	0.676	0.884	0.044	18.944	0.841	0.780	0.863	0.413	9.043
Diamond	0.900	0.835	0.884	0.191	12.611	0.963	0.810	0.957	0.493	7.443
Duck	0.584	0.503	0.588	0.01	18.014	0.684	0.712	0.623	0.044	8.987
Fish	0.915	0.826	0.939	0.437	10.463	0.992	0.782	0.993	0.510	1.850
Gemstone	0.417	0.545	0.454	0.016	11.108	0.534	0.515	0.548	0.007	3.562
Seahorse	0.762	0.817	0.787	0.182	9.655	0.973	0.841	0.972	0.637	1.362
Shell	0.583	0.811	0.646	0.065	11.091	0.881	0.781	0.774	0.086	2.186
Starfish	0.506	0.617	0.491	0.039	10.145	0.652	0.736	0.585	0.048	1.652
Toffees	0.685	0.759	0.721	0.067	12.293	0.929	0.745	0.938	0.347	2.990
Average	0.704	0.705	0.723	0.109	13.022	0.829	0.731	0.813	0.251	4.282

III. EXPERIMENTS

A. Experimental Details

Dataset. Real3D-AD [8] dataset comprises a total of 1,254 samples that are distributed across 12 distinct categories. Each training set for a specific category contains only four samples, similar to the few-shot scenario in 2D anomaly detection. These categories include Airplane, Candybar, Chicken, Diamond, Duck, Fish, Gemstone, Seahorse, Shell, Starfish, and Toffees. All these categories are toys from manufacturing lines. The objects in Real3D-AD dataset have 0.001mm-0.0015mm resolution, 360 degree coverage and perfect prototype.

Baselines. We compare with BTF [14], M3DM [21], PatchCore [9] to evaluate our performance. According to the used point cloud features, they can be grouped into 7 different baselines, namely, BTF (Raw), BTF (FPFH), M3DM (PointMAE), PatchCore (FPFH), PatchCore (FPFH+Raw), PatchCore (PointMAE), PatchCore (PointMAE+RAW), where Raw denotes using coordinate information. PointMAE and FPFH are two different feature descriptors.

Evaluation Metrics. All evaluation metrics are exactly the same as in [8]. We evaluate the object-level anomaly detection performance and the point-level anomaly detection performance via the area under the receiver operator curve (AUROC) and the area under the Precision-Recall curve (AUPR/AP). The higher the AUROC and AUPR, the better anomaly detection performance is. All experiments are conducted on 12th Gen Intel(R) Core(TM) i9-12900K CPU, 64G DDR4 SDRAM and GeForce RTX 3090 platform.

B. Anomaly Detection on Real3D-AD

We compare our method with several methods on Real3D-AD, and Table I shows the anomaly detection results at O-AUROC(object-level AUROC). The FPFH and PointMAE features are combined with Raw feature, respectively. The results indicate that PointMAE-based combination performs better. For the proposed PointCore architecture, the coordinate information of point cloud is indispensable. Table II presents a more comprehensive comparison between our model and the SOTA. PointCore has achieved competitive performance

TABLE III: Mean inference time per object on Real3D-AD.

Method	PointCore	BTF	M3DM	Reg3D-AD
O-AUROC	0.829	0.603	0.552	0.704
P-AUROC	0.731	0.571	0.637	0.705
Time(s)	4.282	3.882	5.061	13.022

TABLE IV: The results obtained from ablation experiments on each module. Baseline represents Reg3D-AD, LO(P-P) represents local optimization based on the point-point ICP algorithm, LO represents local optimization based on the point-plane ICP algorithm, and RB represents Ranking Block.

Method	O-AUROC	P-AUROC	O-AUPR	P-AUPR	Time(s)
Baseline	0.704	0.705	0.723	0.109	13.022
Baseline+LO	0.642	0.635	0.661	0.098	13.531
Baseline+RB	0.734	0.706	0.733	0.127	13.057
Baseline+LO+RB	0.653	0.641	0.679	0.107	13.612
PointCore	0.735	0.716	0.739	0.138	3.929
PointCore+LO	0.796	0.732	0.782	0.226	4.256
PointCore+RB	0.785	0.725	0.763	0.136	3.945
PointCore+LO+RB	0.829	0.731	0.813	0.251	4.282
PointCore+LO(P-P)+RB	0.746	0.618	0.733	0.056	8.314

across all metrics, including a 17.75% improvement in O-AUROC metric. The performance in point-level AUROC (P-AUROC), object-level AUPR (O-AUPR), and point-level AUPR (P-AUPR) further demonstrate the superior performance of our proposal in anomaly detection. The comparisons of inference time among BTF, M3DM and PatchCore are implemented, as tabulated in Table III. As can be seen, BTF presented in Table III, albeit fast, show mediocre to poor performance in O-AUROC and P-AUROC. Ours is the fastest excluding BTF.

C. Ablation Studies

In this section, we ablate our design choices on the Reg3D-AD under 3-view settings in Table. IV.

Effectiveness of Local Optimization (LO). The Reg3D-AD model employs the FPFH+RANSAC method [15] for registration, where the RANSAC algorithm iteratively finds the optimal pose matrix. However, the random points selection

of RANSAC in each iteration leads to significant variance in the final registration results. We conducted 20 experiments on a pair point cloud from the Toffees dataset. The results reveal substantial variations even with identical parameters. The local optimization algorithm is introduced to improve the stability of the registration process. The variance in Euler angles decreased from 1.1058° to $(7.7796 \times 10^{-6})^\circ$, achieving a score of 0.642 ± 0.01 . Regarding the local optimization method, we conduct registration error tests on point-point ICP and point-plane ICP algorithms under different levels of Gaussian noise. The results show that the point-plane ICP registration method often yields more accurate results under lower noise levels. The anomaly samples in the Reg3D-AD dataset resemble a point cloud with low noise levels. The point-plane ICP is chosen as the local optimization method.

Effectiveness of PointCore Architecture. Compared to the Reg3D-AD architecture, PointCore architecture can better leverage the coordinate information of point clouds to achieve faster and more accurate point cloud anomaly detection. Regarding speed, we accelerate the inference process by binding the coordinate information and PointMAE feature information of points. This reduces the substantial computational cost introduced by the subsequent PointMAE searching for nearest neighbors. In contrast, the Reg3D-AD architecture stores the coordinate information and PointMAE feature information separately in different memory banks. Each coordinate and PointMAE must find their nearest neighbors in the corresponding memory bank during inference. This poses a significant computational challenge, especially with the 1154 dimensions of PointMAE feature. Regarding accuracy, we enhance the dominance of coordinate information to avoid obvious mismatches in PointMAE features. Specifically, in the Reg3D-AD architecture, the PointMAE features of test point cloud must find the nearest neighbors in the PointMAE memory bank without utilizing any coordinate information. This process leads to erroneous matches between locally similar groups. By strictly limiting the matching range of coordinates, we significantly reduce the probability of mismatches.

Effectiveness of Ranking Block (RB). From Table. IV, the ranking block significantly improves object-level AUROC and object-level AUPR. However, the improvement in point-level metric is limited. This is because the ranking block is primarily employed to mitigate the substantial impact of outliers on different anomaly score distributions. It plays a significant balancing role for object-level anomaly scores, where the sample size is relatively small. In contrast, point-level anomaly scores inherently have many samples, and the influence of outliers is minimal.

IV. CONCLUSION

We propose an unsupervised point cloud anomaly detector, termed PointCore, which is developed on single memory bank with local-global features to store multi-scale information of input point clouds. Extensive experiments on Real3D-AD dataset demonstrate that ours has better recall rate and lower false-positive rate, which is preferable in real applications requiring precise detection of defective samples. Furthermore,

the proposed framework is efficient since both the local-global feature memory bank and the multi-feature anomaly score calculation reduce the computational cost.

REFERENCES

- [1] D. Carrera, F. Manganini, G. Boracchi, and E. Lanzarone, "Defect detection in sem images of nanofibrous materials," *IEEE Transactions on Industrial Informatics*, p. 551–561, Apr 2017.
- [2] K. Song and Y. Yan, "A noise robust method based on completed local binary patterns for hot-rolled steel strip surface defects," *Applied Surface Science*, p. 858–864, Nov 2013.
- [3] D. Hendrycks, S. Basart, M. Mazeika, M. Mostajabi, J. Steinhardt, and D. Song, "A benchmark for anomaly segmentation," *arXiv preprint arXiv:1911.11132*, vol. 1, no. 2, p. 5, 2019.
- [4] Y. Xu, W. Hu, S. Wang, X. Zhang, S. Wang, S. Ma, Z. Guo, and W. Gao, "Predictive generalized graph fourier transform for attribute compression of dynamic point clouds," *IEEE Transactions on Circuits and Systems for Video Technology*, vol. 31, no. 5, pp. 1968–1982, 2020.
- [5] V. Zavrtnik, M. Kristan, and D. Škočaj, "Draem – a discriminatively trained reconstruction embedding for surface anomaly detection," *International Conference on Computer Vision, International Conference on Computer Vision*, Aug 2021.
- [6] J. T. Zhou, L. Zhang, Z. Fang, J. Du, X. Peng, and Y. Xiao, "Attention-driven loss for anomaly detection in video surveillance," *IEEE transactions on circuits and systems for video technology*, vol. 30, no. 12, pp. 4639–4647, 2019.
- [7] Y. Wang, Q. Liu, and Y. Lei, "Ted-net: Dispersal attention for perceiving interaction region in indirectly-contact hoi detection," *IEEE Transactions on Circuits and Systems for Video Technology*, pp. 1–1, 2024.
- [8] J. Liu, G. Xie, R. Chen, X. Li, J. Wang, Y. Liu, C. Wang, and F. Zheng, "Real3d-ad: A dataset of point cloud anomaly detection," *Advances in Neural Information Processing Systems*, vol. 36, 2024.
- [9] K. Roth, L. Pemula, J. Zepeda, B. Scholkopf, T. Brox, and P. Gehler, "Towards total recall in industrial anomaly detection," in *2022 IEEE/CVF Conference on Computer Vision and Pattern Recognition (CVPR)*, Jun 2022.
- [10] W. Li and X. Xu, "Towards scalable 3d anomaly detection and localization: A benchmark via 3d anomaly synthesis and a self-supervised learning network," *arXiv preprint arXiv:2311.14897*, 2023.
- [11] W. Zhu, Z. Ma, Y. Xu, L. Li, and Z. Li, "View-dependent dynamic point cloud compression," *IEEE Transactions on Circuits and Systems for Video Technology*, vol. 31, no. 2, pp. 765–781, 2020.
- [12] H. Peng and G. Tong, "Class-aware 3d detector from point clouds with partial knowledge diffusion and center-weighted iou," *IEEE Transactions on Circuits and Systems for Video Technology*, 2023.
- [13] H. Xiao, Y. Li, W. Kang, and Q. Wu, "Distinguishing and matching-aware unsupervised point cloud completion," *IEEE Transactions on Circuits and Systems for Video Technology*, 2023.
- [14] E. Horwitz and Y. Hoshen, "Back to the feature: classical 3d features are (almost) all you need for 3d anomaly detection," in *Proceedings of the IEEE/CVF Conference on Computer Vision and Pattern Recognition*, 2023, pp. 2967–2976.
- [15] R. B. Rusu, N. Blodow, and M. Beetz, "Fast point feature histograms (fpfh) for 3d registration," in *2009 IEEE International Conference on Robotics and Automation*, 2009, pp. 3212–3217.
- [16] S. Rusinkiewicz and M. Levoy, "Efficient variants of the icp algorithm," in *Proceedings Third International Conference on 3-D Digital Imaging and Modeling*, 2001, pp. 145–152.
- [17] L. Yang and W. Guo, "Greedy local-set based sampling and reconstruction for band-limited graph signals," in *2016 23rd International Conference on Telecommunications (ICT)*, 2016, pp. 1–5.
- [18] Y. Pang, W. Wang, F. E. Tay, W. Liu, Y. Tian, and L. Yuan, "Masked autoencoders for point cloud self-supervised learning," in *European conference on computer vision*. Springer, 2022, pp. 604–621.
- [19] H. Zhao, L. Jiang, J. Jia, P. Torr, and V. Koltun, "Point transformer," in *2021 IEEE/CVF International Conference on Computer Vision (ICCV)*, Oct 2021.
- [20] A. Chang, T. Funkhouser, L. Guibas, P. Hanrahan, Q. Huang, Z. Li, S. Savarese, M. Savva, S. Song, H. Su, J. Xiao, L. Yi, and F. Yu, "Shapenet: An information-rich 3d model repository," *arXiv: Graphics*, arXiv: Graphics, Dec 2015.
- [21] Y. Wang, J. Peng, J. Zhang, R. Yi, Y. Wang, and C. Wang, "Multimodal industrial anomaly detection via hybrid fusion," in *Proceedings of the IEEE/CVF Conference on Computer Vision and Pattern Recognition*, 2023, pp. 8032–8041.